

Sky localization of space-based detectors with time-delay interferometry

Tong Jiang,^{a,b} Yungui Gong,^{b,c,1} Xuchen Lu^b

^aCollege of Physics and Technology, Kunming University, 2 Puxin Rd, Kunming, Yunnan 650214, China

^bSchool of Physics, Huazhong University of Science and Technology, 1037 LuoYu Rd, Wuhan, Hubei 430074, China

^cInstitute of Fundamental Physics and Quantum Technology, Department of Physics, School of Physical Science and Technology, Ningbo University, 818 Fenghua Rd, Ningbo, Zhejiang 315211, China

E-mail: jiangtong@hust.edu.cn, gongyungui@nbu.edu.cn, Luxc@hust.edu.cn

Abstract. The accurate sky localization of gravitational wave (GW) sources is an important scientific goal for space-based GW detectors. The main differences between future space-based GW detectors, such as Laser Interferometer Space Antenna (LISA), Taiji, and TianQin, include the time-changing orientation of the detector plane, the arm length, the orbital period of the spacecraft and the noise curve. Because of the effects of gravity on three spacecraft, it is impossible to maintain the equality of the arm length, so the time-delay interferometry (TDI) method is needed to cancel out the laser frequency noise for space-based GW detectors. Extending previous work based on equal-arm Michelson interferometer, we explore the impacts of different first-generation TDI combinations and detector's constellations on the sky localization for monochromatic sources. We find that the sky localization power is almost unaffected by the inclusion of the TDI Michelson (X, Y, Z) combination in the analysis. We also find that the variation in the sky localization power for different TDI combinations is entirely driven by the variation in the sensitivities of these combinations. For the six particular TDI combinations studied, the Michelson (X, Y, Z) combination is the best for source localization.

Keywords: Gravitational waves, localization, time-delay interferometry, space-based detectors

ArXiv ePrint: [2301.05923](https://arxiv.org/abs/2301.05923)

¹Corresponding author.

Contents

1	Introduction	1
2	Methodology	2
2.1	The GW signal	3
2.2	The TDI configurations and fiducial detectors	3
2.3	FIM method	7
3	Results	9
3.1	The effects of TDI combinations on sky localization	9
3.2	The effect of network	11
4	Conclusion	12

1 Introduction

The first detection of gravitational waves (GWs) [1] by advanced Laser Interferometer Gravitational-Wave Observatory (LIGO) Scientific Collaboration [2, 3] and Virgo Collaboration [4] opened a new window to test Einstein’s general relativity [5–8], study the population of stellar-mass black holes, measure the merger rates of binary black holes in the Universe, probe the evolution history of the Universe and understand the nature of the gravity [9–20]. However, the ground-based GW observatories are only sensitive to GWs in the high frequency bands $10 - 10^3$ Hz due to seismic noise and gravity gradient noise. The proposed space-based GW detectors such as Laser Interferometer Space Antenna (LISA) [21, 22], Taiji [23], and TianQin [24] will detect GWs in the low frequency regimes $10^{-4} - 10^{-1}$ Hz where a wealth of astrophysical sources resides. Accurate sky localization is an important scientific goal for GW observations [25]. The accurate information about the source localization is essential for the follow-up observations of electromagnetic counterparts and the statistical identification of the host galaxy when no counterpart is present [25–27], so that GWs can be used as standard sirens [28, 29] to probe the evolution of the Universe and study the problem of the Hubble tension [30–35]. Moreover, accurate knowledge about the GW source position may provide important information about the environments where the binary source resides. However, the errors in determining the source position are strongly correlated with the other parameters of the binary source [26, 36, 37], so accurate source localization depends on the GW detector and the type of source. In contrast to the coalescing signals detectable by ground-based detectors, space-based GW detectors can measure monochromatic GWs from short-period binary stars for months to years, and the translatory motion of detector’s center around the Sun imposes on the signal a periodic Doppler shift, the Doppler modulation on the amplitude and phase of GWs carries the position information of the sources. Therefore, a single space-based GW detector is able to locate the source position.

There are two different constellations for space-based GW detectors. For LISA/Taiji, the spacecraft is in the heliocentric orbit behind/ahead of the Earth by about 20° , the inclination angle between the plane of constellations and ecliptic plane is 60° , and they keep the geometry of an almost equilateral triangle with the average arm length $L = 2.5 \times 10^9$ m/ 3×10^9 m. For TianQin, the spacecraft is in the geocentric orbit around the Earth and

rotates around the Sun, the arm length is $L = 1.73 \times 10^8$ m, and the normal vector of the detector plane points to the source RX J0806.3+1527 at $(\theta_{tq} = -4.7^\circ, \phi_{tq} = 120.5^\circ)$. The main differences between different constellations of space-based GW detectors are the time-changing orientation of the detector plane, the arm length, the orbital period of the spacecraft and the noise curve [38]. It is necessary to discuss the effects of these factors on the accuracy of source localization.

As discussed in [38–40] for monochromatic sources, the source-position-dependent modulation on the signal amplitude due to the rotation of the detector plane with a period of one year which dominates over the Doppler modulation at frequencies below 1mHz, not only helps LISA and Taiji get better accuracy in the sky localization of GW source but also increases the sky coverage at frequencies below 1mHz [26, 36, 38–41]. The ability in the sky localization of TianQin is better than LISA and Taiji at frequencies above 30 mHz and TianQin has blind spots for sources from the directions with ϕ_s around 30° or -150° . At higher frequencies when the wavelength of GWs is smaller than the detector’s arm length, the frequency-dependent transfer function deteriorates the signal-to-noise ratio (SNR) registered in the detector. Compared to the individual detectors, the network of LISA and TianQin has a better ability in sky localization for sources with frequencies in the range of 1-100 mHz and offers larger sky coverage for angular resolutions.

The motion of spacecraft in space makes space-based GW detectors impossible to maintain the exact equality between the arm lengths. Because of the unequal arm lengths, the laser frequency noise cannot be cancelled out completely. To reduce the laser frequency noise, properly chosen time shifted and linearly combined data streams were proposed to synthesize virtual equal arm interferometric measurements [42–44]. This technique is known as time-delay interferometry (TDI) [43–47]. The first-generation TDI combinations can cancel out the laser frequency noise in a static unequal-arm configuration, and the second-generation TDI can cancel out the laser frequency noise in a rotating and flexing configuration with arm lengths varying linearly in time [46, 48, 49]. The first-generation TDI configurations were applied for space-based GW detectors such as LISA, Taiji and TianQin in [45, 48, 50–60], and the applications of second-generation TDI configurations were discussed in [46, 47, 49, 61–67]. For more discussion on TDI algorithm and its application to space-based GW detectors, please see [68–71] and references therein. Since the noises in different TDI combinations are different, we expect that the ability of sky localization with different TDI combinations will be different. Thus, we extend previous work to study the effect of different TDI combinations on the sky localization.

The paper is organized as follows. In Sec. 2, we provide a brief overview of TDI response and Fisher information matrix (FIM) method. In Sec. 3, we consider five fiducial detectors and six particular TDI combinations to discuss the effects of different TDI combinations and constellation factors on the sky localization for monochromatic GWs, and compare the results of angular resolutions between LISA, Taiji, TianQin, and their network. Finally, we present the discussion in Sec. 4.

2 Methodology

In this section, we provide a brief overview on TDI responses of space-based GW detectors to monochromatic GWs and parameter estimations with the method of FIM.

2.1 The GW signal

For GWs propagating along the direction $\hat{\Omega}(\theta, \phi)$, we can define two perpendicular unit vectors \hat{p} and \hat{q} that satisfy the orthogonal relation $\hat{\Omega} = \hat{p} \times \hat{q}$. To account for the rotational degree of freedom around $\hat{\Omega}$, we introduce the polarization angle ψ to form two new orthonormal vectors

$$\hat{r} = \cos(\psi)\hat{p} + \sin(\psi)\hat{q}, \quad \hat{s} = -\sin(\psi)\hat{p} + \cos(\psi)\hat{q}. \quad (2.1)$$

With these two orthonormal bases, the plus (+) and cross (\times) polarization tensors are

$$e_{ij}^+ = \hat{r}_i \hat{r}_j - \hat{s}_i \hat{s}_j, \quad e_{ij}^\times = \hat{r}_i \hat{s}_j + \hat{r}_j \hat{s}_i, \quad (2.2)$$

and the GW signal can be expressed as

$$h_{ij}(t) = \sum_{A=+, \times} e_{ij}^A h_A(t). \quad (2.3)$$

For monochromatic GWs with the frequency f_0 emitted from sources such as compact binaries containing stellar or intermediate-mass black holes, white dwarfs or neutron stars, in the lowest order of quadrupole approximation the tensor modes are

$$\begin{aligned} h_+(t) &= \mathcal{A}[1 + \cos^2(\iota)]e^{(2\pi i f_0 t + i\phi_0)}, \\ h_\times(t) &= 2i\mathcal{A}\cos^2(\iota)e^{(2\pi i f_0 t + i\phi_0)}, \end{aligned} \quad (2.4)$$

where the amplitude $\mathcal{A} = 2m_1 m_2 (\pi f_0)^{2/3} / [(m_1 + m_2)^{1/3} d_L]$, m_1 and m_2 are masses of the binary components, d_L is the luminosity distance between the source and the observer, ϕ_0 is the initial phase of the orbital plane and ι is the inclination angle of the detector plane. The signal registered in the detector α is

$$z_\alpha(t) = \sum_A F_\alpha^A(f, \theta, \phi, \psi) h_A(t) e^{i\phi_D(t)} + n_\alpha(t), \quad (2.5)$$

where $n_\alpha(t)$ is the detector noise, $\phi_D(t)$ is the Doppler phase, and the $F_\alpha^A(f, \theta, \phi, \psi)$ is the response function in the detector α [45]. For GW signals with the frequency f_0 , the Doppler phase is

$$\phi_D(t) = 2\pi f_0 R_s \sin \theta \cos \left(\frac{2\pi t}{P} - \phi - \phi_\alpha \right), \quad (2.6)$$

where $R_s = 1$ AU is the distance between the sun and the earth, θ and ϕ are the angular position of the GW source in the ecliptic coordinate, P is the period of rotation for the earth around the sun, and ϕ_α is the detector's ecliptic longitude at $t = 0$, so the source parameters are $\mathbf{\Lambda} = (\theta, \phi, \mathcal{A}, \iota, \psi, \phi_0)$.

2.2 The TDI configurations and fiducial detectors

For space-based GW detectors, it is impossible to maintain the exact equality of the arm lengths due to the motion of spacecraft (SC), so laser frequency noise cannot be effectively removed when two beams are recombined directly at the photo-detector. Fortunately, we can form, from the multiple readouts of space-based GW detectors, observables that are insensitive to laser frequency fluctuations and optical bench motions by properly choosing time shifted and linearly combined data streams. This technique is known as TDI. Although there are numerous TDI combinations [71] which can be derived from the four generators

$(\alpha, \beta, \gamma, \zeta)$ [54], we focus on six particular TDI combinations [68–70] in this paper. As shown in figure 1, these six combinations for the first-generation TDI are Sagnac ζ , six-pulse (α, β, γ) , Michelson (X, Y, Z) , Relay (U, V, W) , Beacon (P, Q, R) , and monitor (E, F, G) . In figure 1, the spacecraft are labeled as 1, 2, 3, the optical paths between two SCs are denoted by L_a which are assumed to be constant for the discussion of the first-generation TDI combinations, the index a corresponds to the opposite SC $_a$ and $a = 1, 2, 3$. The three channels of each configuration are obtained by cyclical permutation of the spacecraft indices.

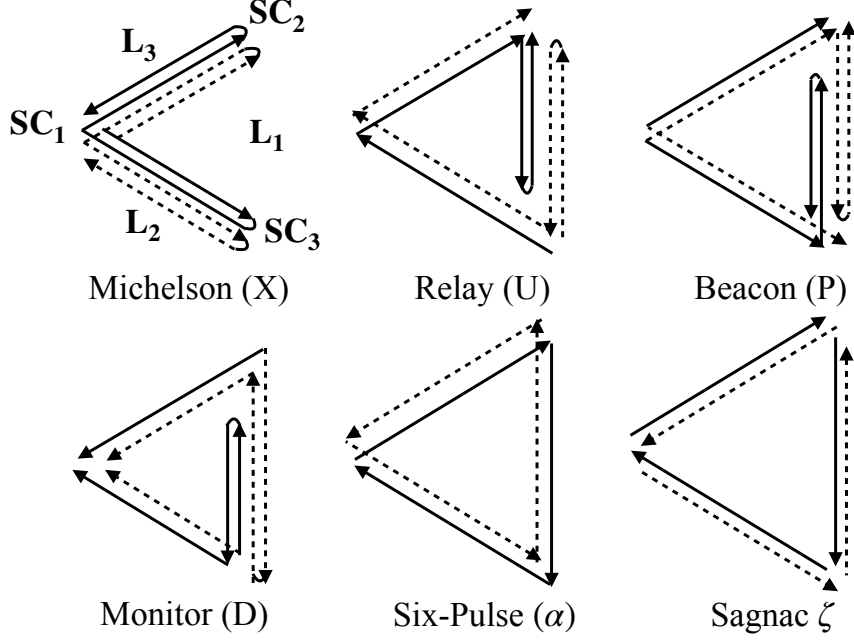


Figure 1. The configurations of six first-generation TDI combinations [45, 62].

For the response of the one-way transmission, as shown in figure 2, between SC $_3$ and SC $_2$ with the distance L_1 along the unit direction \hat{n}_1 is [72]

$$\begin{aligned} \delta L_1 &= \sum_{A,i,j} \hat{n}_1^i \hat{n}_1^j e_{ij}^A \frac{\sin[\omega L_1(1 - \hat{n}_1 \cdot \hat{\Omega})/2]}{\omega(1 - \hat{n}_1 \cdot \hat{\Omega})} e^{-i\omega L_1(1 - \hat{n}_1 \cdot \hat{\Omega} + 2\Omega \cdot \vec{r}_2/L_1)/2} h^A(f) \\ &= \sum_{A,i,j} L_1 \hat{n}_1^i \hat{n}_1^j e_{ij}^A T(\omega, \hat{n}_1 \cdot \hat{\Omega}) h^A(f), \end{aligned} \quad (2.7)$$

where $\omega = 2\pi f$ is the angular frequency of GWs, $\hat{\Omega}$ is the propagating direction of GWs. We take the speed of light $c = 1$. The transfer function $T(\omega, \hat{n}_1 \cdot \hat{\Omega})$ is [73]

$$\begin{aligned} T(\omega, \hat{n}_1 \cdot \hat{\Omega}) &= \frac{\sin[\omega L_1(1 - \hat{n}_1 \cdot \hat{\Omega})/2]}{\omega L_1(1 - \hat{n}_1 \cdot \hat{\Omega})} e^{-i\omega L_1(1 - \hat{n}_1 \cdot \hat{\Omega} + 2\Omega \cdot \vec{r}_2/L_1)/2} \\ &= \frac{1}{2} \text{sinc} \left[\omega L_1(1 - \hat{n}_1 \cdot \hat{\Omega})/2 \right] e^{-i\omega L_1(1 - \hat{n}_1 \cdot \hat{\Omega} + 2\Omega \cdot \vec{r}_2/L_1)/2}, \end{aligned} \quad (2.8)$$

where $\text{sinc}(x) = \sin x/x$ and \vec{r}_2 is the location of SC $_2$. In the long-wavelength limit, $\omega L_1 \rightarrow 0$, $\text{sinc} \left[\omega L_1(1 - \hat{n}_1 \cdot \hat{\Omega})/2 \right] \approx 1$ which is independent of the GW frequency.

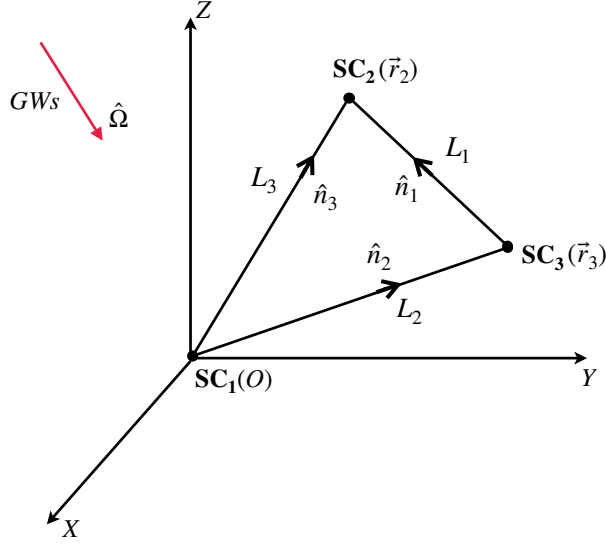


Figure 2. The one-way Doppler tracking. We put SC_1 at the origin of the coordinate, the other two spacecraft SC_2 and SC_3 are located at \vec{r}_2 and \vec{r}_3 . GWs propagate along the direction $\hat{\Omega}$, the optical paths between two SC pairs are denoted by L_a and the unit vectors along the path are \hat{n}_a , with the index a corresponding to the opposite SC.

Following [44], we denote y_{ab} as the relative frequency fluctuations time series measured from reception at SC_b with transmission from SC_d ($d \neq a$ and $d \neq b$) along L_a , for example, y_{31} is the relative frequency fluctuations time series measured at spacecraft 1 with transmission from spacecraft 2 along L_3 ; we also use the notation $y_{ab,c}$ for the delayed data stream, for example, $y_{31,2} = y_{31}(t - L_2)$ and $y_{31,32} = y_{31}(t - L_3 - L_2)$. By using Eqs. (2.7) and (2.8), the six TDI signal responses of GW are

$$\begin{aligned}
y_{ab}(T_D) &= -\frac{\delta L_a}{L_a} = -\sum_{A,i,j} \hat{n}_a^i \hat{n}_a^j e_{ij}^A T_{ab}(T_D) h^A(f), \\
T_{12}(T_D) &= \frac{1}{2} \text{sinc} \left[\frac{1}{2} u_1 (1 - \mu_1) \right] e^{-iu_1(1-\mu_1)/2 - i(\mu_3 u_3 + T_D)}, \\
T_{23}(T_D) &= \frac{1}{2} \text{sinc} \left[\frac{1}{2} u_2 (1 - \mu_2) \right] e^{-iu_2(1-\mu_2)/2 - i(\mu_2 u_2 + T_D)}, \\
T_{32}(T_D) &= \frac{1}{2} \text{sinc} \left[\frac{1}{2} u_3 (1 - \mu_3) \right] e^{-iu_3(1-\mu_3)/2 - i(\mu_3 u_3 + T_D)}, \\
T_{31}(T_D) &= \frac{1}{2} \text{sinc} \left[\frac{1}{2} u_3 (1 + \mu_3) \right] e^{-iu_3(1+\mu_3)/2 - iT_D}, \\
T_{13}(T_D) &= \frac{1}{2} \text{sinc} \left[\frac{1}{2} u_1 (1 + \mu_1) \right] e^{-iu_1(1+\mu_1)/2 - i(\mu_2 u_2 + T_D)}, \\
T_{21}(T_D) &= \frac{1}{2} \text{sinc} \left[\frac{1}{2} u_2 (1 + \mu_2) \right] e^{-iu_2(1+\mu_2)/2 - iT_D},
\end{aligned} \tag{2.9}$$

where $u_a = (2\pi f)L_a$, $\mu_a = \hat{n}_a \cdot \hat{\Omega}$, T_D is the corresponding time delay, for example, $T_D = u_1 + u_2$ for $y_{ab,12}$. The response function $F^A(f, \theta, \phi, \psi) = \hat{n}_a^i \hat{n}_a^j e_{ij}^A T_{ab}(T_D)$.

Due to the cancellation of frequency noises in the stationary unequal-arm interferometry by the first-generation TDI combinations, the dominant detector noises are the acceleration noise and the single-link optical metrology noise. The acceleration noises for LISA [74] and Taiji [64] are

$$S_{\text{LISA}}^a = S_{\text{TJ}}^a = (3 \times 10^{-15} \text{ m s}^{-2})^2 \left[1 + \left(\frac{0.4 \text{ mHz}}{f} \right)^2 \right] \left[1 + \left(\frac{f}{8 \text{ mHz}} \right)^4 \right] \text{ Hz}^{-1}, \quad (2.10)$$

the single-link optical metrology noises for LISA and Taiji are

$$\begin{aligned} S_{\text{LISA}}^x &= (1.5 \times 10^{-11} \text{ m})^2 \left[1 + \left(\frac{2 \text{ mHz}}{f} \right)^4 \right] \text{ Hz}^{-1}, \\ S_{\text{TJ}}^x &= (8 \times 10^{-12} \text{ m})^2 \left[1 + \left(\frac{2 \text{ mHz}}{f} \right)^4 \right] \text{ Hz}^{-1}, \end{aligned} \quad (2.11)$$

respectively. The acceleration noise and the single-link optical metrology noise for TianQin are [24]

$$\begin{aligned} S_{\text{TQ}}^a &= 10^{-30} \text{ m}^2 \text{ s}^{-4} / \text{Hz}, \\ S_{\text{TQ}}^x &= 10^{-24} \text{ m}^2 / \text{Hz}. \end{aligned} \quad (2.12)$$

For an equal-arm detector with the arm length L , the fractional frequency fluctuation spectra for the shot and proof mass noises are related to the single-link optical metrology and acceleration noises as [44, 45]

$$\begin{aligned} S_y^{\text{shot}} &= S^x / L^2, \\ S_y^{\text{proof mass}} &= S^a / (L^2 (2\pi f)^4), \end{aligned} \quad (2.13)$$

where the subscript y represents the individual laser link y_{ab} . For LISA, $L = 2.5 \times 10^9$ m; for Taiji, $L = 3 \times 10^9$ m; and for TianQin, $L = 1.78 \times 10^8$ m. For the space-based GW detectors, the three laser arms are treated as two Michelson interferometers during the detection process, with one laser arm being shared by both. This introduces correlation issues in signal analysis, causing the noise to become partially correlated [54, 69, 75, 76]. However, the impact of noise correlation is the higher-order effect in measurement, even though the difference of the power spectral density of noise between full-correlated and none correlated noises is similar in the case of Michelson (X, Y, Z) combination [77]. Therefore, in this paper, we simplify the calculation by treating the noise performance as the uncorrelated single-link contribution from the optical measurement system and test-mass acceleration.

The noises in different TDI combinations are [45]

$$P_n^\alpha = [8 \sin^2(3\pi fL) + 16 \sin^2(\pi fL)] S_y^{\text{proof mass}} + 6 S_y^{\text{shot}}, \quad (2.14)$$

$$P_n^\zeta = 24 \sin^2(\pi fL) S_y^{\text{proof mass}} + 6 S_y^{\text{shot}}, \quad (2.15)$$

$$P_n^X = [8 \sin^2(4\pi fL) + 32 \sin^2(2\pi fL)] S_y^{\text{proof mass}} + 16 \sin^2(2\pi fL) S_y^{\text{shot}}, \quad (2.16)$$

$$P_n^P = [8 \sin^2(2\pi fL) + 32 \sin^2(\pi fL)] S_y^{\text{proof mass}} + [8 \sin^2(2\pi fL) + 8 \sin^2(\pi fL)] S_y^{\text{shot}}, \quad (2.17)$$

Detector	R	C	R1	C1	C2
Arm Length (m)	3.7×10^9	3.7×10^9	1.73×10^8	1.73×10^8	1.73×10^8
Period	1 year	1 year	1 year	1 year	3.65 days

Table 1. The parameters of the fiducial detectors. The LISA-like fiducial detectors R and R1 are in the heliocentric orbit, the TianQin-like fiducial detectors C, C1 and C2 are in the geocentric orbit and their normal vectors of the detector planes point to the calibration source RX J0806.3+1527.

$$P_n^E = [32 \sin^2(\pi fL) + 8 \sin^2(2\pi fL)]S_y^{\text{proof mass}} + [8 \sin^2(\pi fL) + 8 \sin^2(2\pi fL)]S_y^{\text{shot}}, \quad (2.18)$$

$$P_n^U = [16 \sin^2(\pi fL) + 8 \sin^2(2\pi fL) + 16 \sin^2(3\pi fL)]S_y^{\text{proof mass}} + [4 \sin^2(\pi fL) + 8 \sin^2(2\pi fL) + 4 \sin^2(3\pi fL)]S_y^{\text{shot}}. \quad (2.19)$$

Since GWs come from all directions, we use the average response function $R(f)$ by taking the average of the response function F^A over all source directions and the polarization angle [78]. The sensitivity curve is $S_n(f) = P_n(f)/R(f)$.

For different constellations of space-based GW detectors, three dominant design factors affect the accuracy of source localization: the rotation, the arm length, and the rotation period of the spacecraft [38]. To examine the effects of these factors individually, we use the control variable method and construct five fiducial GW detectors as shown in table 1 [38]. The LISA-like fiducial detectors R and R1 are in the heliocentric orbit with the orbital period of one year and the normal vector of the detector plane rotates around the normal vector of the ecliptic plane with a period of one year. The TianQin-like fiducial detectors C, C1 and C2 are in the geocentric orbit and the normal vector of the detector plane points to the calibration source RX J0806.3+1527. The orbital period of the fiducial detectors C and C1 is one year while the orbital period of the fiducial detector C2 is 3.65 days. The detailed orbit equations for these fiducial detectors were given in Ref. [38]. The fiducial detector R (R1) and C (C1) are constructed to study the effect of rotation, the fiducial detector R (C) and R1 (C1) are constructed to study the effect of the arm length, and the fiducial detector C1 and C2 are constructed to study the effect of the rotation period of the spacecraft. For all fiducial detectors, we assume that the acceleration noise and the single-link optical metrology noise are the same as LISA. In figure 3, we plot $\sqrt{S_n(f)}$ of LISA and the fiducial detector C1 for the tensor modes for the six TDI combinations. From figure 3, we see that the Sagnac combination ζ suppresses the GW signals because its response to GWs becomes of higher order [44], especially below 0.1 Hz, so we expect that the sky localization will be very bad with the ζ combination.

2.3 FIM method

Given two frequency-domain signals $h_1(f)$ and $h_2(f)$, the inner product $\langle h_1|h_2 \rangle$ is defined as

$$\langle h_1|h_2 \rangle = 2 \int_0^{+\infty} \frac{h_1(f)h_2^*(f) + h_2(f)h_1^*(f)}{P_n(f)} df, \quad (2.20)$$

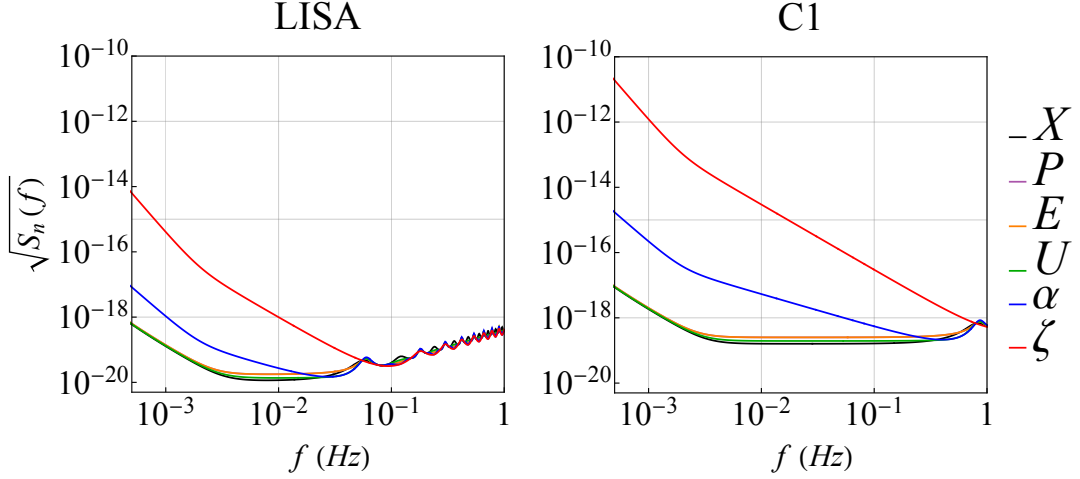


Figure 3. The sensitivity curves $\sqrt{S_n(f)}$ of LISA and C1 for the six TDI combinations for the tensor modes.

where h^* denotes the complex conjugate of h . The SNR of GW signal z_α is

$$\begin{aligned} \rho^2 &= \langle z_\alpha | z_\alpha \rangle \\ &= 4 \int_0^\infty \frac{z_\alpha(f) z_\alpha^*(f)}{P_n^\alpha(f)} df. \end{aligned} \quad (2.21)$$

In this paper, we choose the threshold of detecting a signal as $\rho \geq 10$. To estimate the uncertainty of source parameters, we apply the FIM method. The FIM is defined as

$$\begin{aligned} \Gamma_{ij} &= \left\langle \frac{\partial z_\alpha}{\partial \mathbf{\Lambda}_i} \middle| \frac{\partial z_\alpha^*}{\partial \mathbf{\Lambda}_j} \right\rangle \\ &= 4 \operatorname{Re} \int_0^\infty \frac{\partial_i z_\alpha(f) \partial_j z_\alpha^*(f)}{P_n^\alpha(f)} df \\ &= \frac{2}{P_n^\alpha(f)} \operatorname{Re} \int_{-\infty}^\infty \partial_i z_\alpha(t) \partial_j z_\alpha^*(t) dt, \end{aligned} \quad (2.22)$$

where α represents the TDI channel, $\partial_i z_\alpha = \partial z_\alpha / \partial \mathbf{\Lambda}_i$ and $\mathbf{\Lambda}_i$ is the i th parameter of GW source. For monochromatic sources with the frequency f , because there is almost no frequency evolution, by using Parseval's theorem [26, 79] the noise function $P_n^\alpha(f)$ can be taken out from the integration. The covariance matrix σ_{ij} between the parameters errors $\Delta \mathbf{\Lambda}_i = \mathbf{\Lambda}_i - \langle \mathbf{\Lambda}_i \rangle$ and $\Delta \mathbf{\Lambda}_j$ can be approximated by the inverse of the Fisher matrix in the large SNR limit,

$$\sigma_{ij} = \langle \Delta \mathbf{\Lambda}_i \Delta \mathbf{\Lambda}_j \rangle \approx (\Gamma^{-1})_{ij}. \quad (2.23)$$

The angular uncertainty of the sky localization is defined as

$$\Delta \Omega_s = 2\pi |\sin \theta| \sqrt{\sigma_{\theta\theta} \sigma_{\phi\phi} - \sigma_{\theta\phi}^2}. \quad (2.24)$$

For a network of n detectors, the SNR and FIM are defined as $\rho^2 = \sum_{\alpha=1}^n \rho_\alpha^2$ and $\Gamma_{ij} = \sum_{\alpha=1}^n \Gamma_{ij}^\alpha$, respectively.

		The mean value of $\Delta\Omega_s$				
f (Hz)	R	C	R1	C1	C2	
0.001	1.0920×10^{-3}	2.4432×10^{-3}	5.1626×10^{-1}	1.1256	1.1293	
0.01	1.9150×10^{-5}	2.1554×10^{-5}	7.4818×10^{-3}	8.0221×10^{-3}	8.0474×10^{-3}	
0.1	2.6030×10^{-7}	2.7312×10^{-7}	5.9204×10^{-6}	5.5359×10^{-6}	5.5201×10^{-6}	
		The median value of $\Delta\Omega_s$				
f (Hz)	R	C	R1	C1	C2	
0.001	1.0996×10^{-3}	1.3618×10^{-3}	5.1946×10^{-1}	6.3687×10^{-1}	6.3901×10^{-1}	
0.01	1.3494×10^{-5}	1.1919×10^{-5}	5.4821×10^{-3}	4.5385×10^{-3}	4.5536×10^{-3}	
0.1	1.3888×10^{-7}	1.4228×10^{-7}	3.7552×10^{-6}	3.1334×10^{-6}	3.1142×10^{-6}	

Table 2. The mean and median values of the angular resolutions $\Delta\Omega_s$ for different fiducial detectors without TDI.

3 Results

In this section, we show the results of angular resolutions with different fiducial detectors using six TDI combinations and discuss the impacts of different TDI combinations and detector constellations on the sky localization for monochromatic sources.

We simulate 3600 GW sources with six parameters $\mathbf{\Lambda} = (\theta, \phi, \mathcal{A}, \iota, \psi, \phi_0)$, where θ and ϕ are chosen randomly in $[-\pi/2, \pi/2]$ and $[-\pi, \pi]$, $\iota = 1$ radian, $\psi = \phi_0 = 0$. Following Ref. [38], we fix the amplitude \mathcal{A} by considering sources with the same masses and distance randomly distributed in the sky. We take the sources to be equal mass binary system with the total mass $(6, 3 \times 10^2, 10^4)M_\odot$ at the distance $(2.3, 1.3 \times 10^3, 10^4)$ Mpc so that the minimum SNR $\rho > 10$, the corresponding GW frequencies are $(10^{-1}, 10^{-2}, 10^{-3})$ Hz, respectively. The benchmark frequencies $f_0 = 1$ mHz, $f_0 = 0.01$ Hz and $f_0 = 0.1$ Hz represent the relative low, medium and high frequency regions.

The mean and median values of the angular resolutions without TDI are shown in table 2. In figure 4, we show the mean as well as the 1σ values of the ratio of the angular resolutions with TDI combinations to those without TDI for the fiducial detectors R and C1. The mean and the 1σ values of the ratio of the angular resolutions between two fiducial detectors are shown in figure 5. We also plot the ratio of the sensitivity curves between the two fiducial detectors R1 and R with and without TDI at the three benchmark frequencies in figure 5. The sensitivity curves of LISA, Taiji and TianQin with the Michelson (X, Y, Z) combination are shown in figure 6. For space-based GW detectors LISA, Taiji and TianQin and the LISA-Taiji-TianQin network with the Michelson X combination, the mean and median values of the angular resolutions are shown in table 3, the sky maps of the angular resolutions are shown in figure 7.

3.1 The effects of TDI combinations on sky localization

To explore the effects of TDI combinations on the sky localization, we calculate the angular resolutions of different fiducial detectors with and without TDI. The mean and median values of the angular resolutions without TDI are shown in table 2. The results without TDI can be regarded as a baseline for comparison. The mean and the 1σ values of the ratio between the angular resolutions with and without TDI for the fiducial detectors R and C1 are shown in figure 4. Since the results for the other fiducial detectors are similar, we don't show them in figure 4. As shown in figure 3, for the fiducial detectors R and C, the (X, Y, Z) combination

has better sensitivities at medium and low frequencies, we expect better sky localization with the (X, Y, Z) combination than the other TDI combinations. At the low frequency $f_0 = 1$ mHz, the sensitivity $S_n(f)$ with α and ζ combinations is larger by a few orders of magnitude, so the angular resolutions are much worse. In fact, for the choices of parameters given above, the sources cannot be detected with α and ζ combinations because their SNRs are too small. At the frequency $f_0 = 0.1$ Hz, the difference between the sensitivities for the six TDI combinations is less than 5%, so difference between the angular resolutions with different TDI combinations is also less than 5%. The results for the angular resolutions with the fiducial detectors R and C are consistent with these expectations. For the fiducial detectors R1, C1 and C2, the (X, Y, Z) combination has better sensitivities at frequencies $f_0 \leq 0.1$ Hz, so the sky localization with the (X, Y, Z) combination is better than the other TDI combinations as shown in figure 4.

For the fiducial detector R, at $f_0 = 0.1$ Hz, the ratios between the mean values of the angular resolutions with and without TDI for all TDI combinations are no more than 1.39; at $f_0 = 0.01$ Hz, the ratios for the X , P , E , U and α combinations are less than 2.55, but the ratio reaches 8.8×10^2 for the ζ combination; at $f_0 = 1$ mHz, the ratios for the X , P , E , and U combinations are less than 2.55, the ratios for the α and ζ combinations are 32 and 7.4×10^5 , respectively. For the fiducial detector C1, the ratios for the X , P , E , and U combinations are all within 2.17, but the ratios for the α and ζ combinations are much larger. In fact, the ratio between the mean values of the angular resolutions with and without TDI for all TDI combinations equals to the ratio of the sensitivities $S_n^{\text{TDI}}/S_n^{\text{no-TDI}}$. The results explain why the sky localization with the (X, Y, Z) combination is better. As shown in figure 4, the sky localization with the Sagnac combination ζ is much worse because its response to GWs becomes of higher order [44], so we don't consider the ζ combination in the discussion below.

To explore the effects of the constellations on the sky localization with different TDI combinations, we show the mean and 1σ values of the ratios of the angular resolutions between the fiducial detectors R and C, C1 and C2, R1 and R for different TDI combinations in figure 5. Comparing the results between R and C as shown in the upper left panel of figure 5, we see that the rotation of the normal vector to the detector plane helps improve the mean value of the angular resolutions by a factor ~ 2 at $f_0 = 1$ mHz and the effect of the detector's changing orientation is negligible at $f_0 = 0.01$ Hz and $f_0 = 0.1$ Hz. The results for the effects of the rotation of the normal vector to the detector plane on the angular resolutions are the same as those found in Ref. [38]. The effect of the detector's changing orientation on the sky localization is similar regardless of TDI combinations (the difference between different TDI combinations is less than 8% at $f_0 = 1$ mHz, 2% at $f_0 = 0.01$ Hz and $f_0 = 0.1$ Hz.), i.e., the ratio of the mean values of the angular resolutions between the fiducial detectors C and R is approximately 2.24 at $f_0 = 1$ mHz, 1.1 at $f_0 = 0.01$ Hz and $f_0 = 0.1$ Hz for all TDI combinations and no-TDI. To see the effect of the orbital period, following Ref. [38] we compare the fiducial detectors C1 and C2 and the results are shown in the upper right panel of figure 5. As found in [38], the influence of the rotation period of the spacecraft for the sky localization is almost negligible. The ratio of the angular resolutions between the fiducial detectors C1 and C2 is approximately 1 at the three benchmark frequencies for all TDI combinations, the difference between different TDI combinations is less than 1% at all three frequencies except the P combination which is about 23.7% at $f_0 = 1$ mHz.

The arm length affects both the noise and the transfer function of the detectors, so the angular resolutions for detectors with different arm lengths depend on the sensitivity curve.

For better understanding of the result, we also show the ratios of the sensitivity curves between the fiducial detectors R and R1 with and without TDI at the three benchmark frequencies in figure 5. The results in figure 5 show that with detectors 1 and 2, the ratio between the angular resolutions $\Delta\Omega_{s,1}/\Delta\Omega_{s,2} = S_{n,1}/S_{n,2}$ for all TDI combinations. Since the influence of different TDI combination on the sky localization mainly comes from the sensitivity curve of the detector with the TDI combination and the (X, Y, Z) combination has better sensitivity, therefore we consider the (X, Y, Z) combination only in the next section.

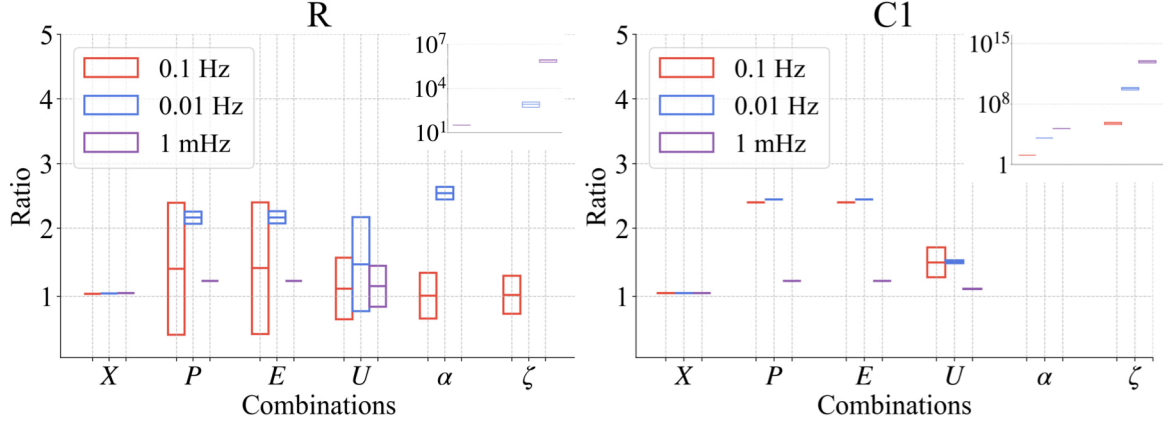


Figure 4. The mean and the 1σ values of the ratio of the angular resolutions with TDI combinations to those without TDI for the fiducial detectors R and C1. The colored boxes and the horizontal lines represent 1σ and the mean values of the ratio of the angular resolutions, respectively. The left panel is for the fiducial detector R and the right panel is for the fiducial detector C1. The angular resolutions are worse if the ratio is larger than 1. The inserts show the huge ratios with α and ζ combinations.

3.2 The effect of network

In this subsection, we apply the TDI (X, Y, Z) combination to discuss the ability of sky localization for space-based GW detectors LISA, Taiji and TianQin and the LISA-Taiji-TianQin network. The sensitivity curves of LISA, Taiji and TianQin with the Michelson (X, Y, Z) combination are shown in figure 6. The mean and median values of angular resolutions are shown in table 3. In table 3 we also show the mean and median values of angular resolutions for space-based GW detectors and their network without applying the TDI method. The sky map of angular resolutions is shown in figure 7.

At the frequency $f_0 = 1$ mHz, the amplitude modulation helps LISA and Taiji on improving the sky localization and there is no equatorial pattern in the sky map. For the sky localization, LISA is better than TianQin by about 34 times, Taiji is two times better than LISA, and the LISA-Taiji-TianQin network is 2.5 times better than Taiji. At the relative medium and high frequencies $f_0 = 0.01$ Hz and $f_0 = 0.1$ Hz, the amplitude modulation is negligible and the Doppler modulation dominates, the equatorial pattern exists in the sky map as shown in figure 7.

At the medium frequency $f_0 = 0.01$ Hz, the GW wavelength is still bigger than the arm length of LISA and Taiji; for the sky localization, LISA is less than two times better than TianQin, Taiji is almost five times better than LISA, and the LISA-Taiji-TianQin network is less than two times better than Taiji.

As the frequency of GWs increases, the wavelength of GWs becomes shorter. When the wavelength of GWs is shorter than detector's arm length, the frequency-dependent transfer

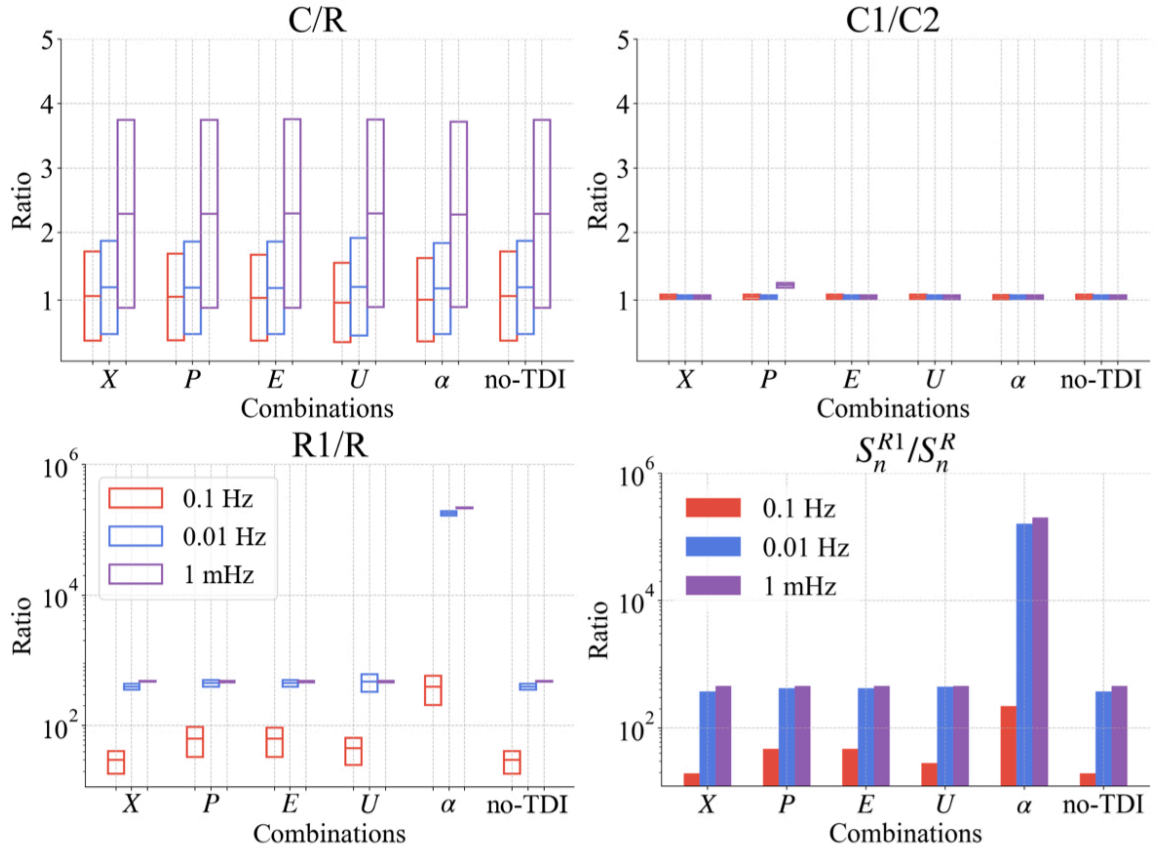


Figure 5. The mean and the 1σ values of the ratio of the angular resolutions between two fiducial detectors with different TDI combinations. The colored boxes and the horizontal lines represent 1σ and the mean values of the ratio of the angular resolutions, respectively. The ratio of the sensitivity curves between the fiducial detectors R and R1 with and without TDI at the three benchmark frequencies is shown in the bottom right panel.

function can deteriorate the SNR registered in the detector. At the relatively high frequency $f_0 = 0.1$ Hz, the GW wavelength is smaller than the arm length of LISA and Taiji, but bigger than the arm length of TianQin, so TianQin has a better ability of sky localization than LISA and Taiji. For the sky localization, Taiji is two times better than LISA, TianQin is seven times better than Taiji, and the LISA-Taiji-TianQin network is around ten times better than Taiji.

For monochromatic sources, the detector in different orbital positions can be thought as an independent detector, so the improvement on the angular resolutions by the network of combined detectors is small.

4 Conclusion

For spaced-based GW detectors, the technique of TDI is needed to cancel out laser frequency noises due to the difficulty of maintaining the exact equality of the arm length in space. We extend the previous work on the analysis of the main factors that influence the accuracy of source localization by considering six particular TDI combinations and discussing their effects on the sky localization.

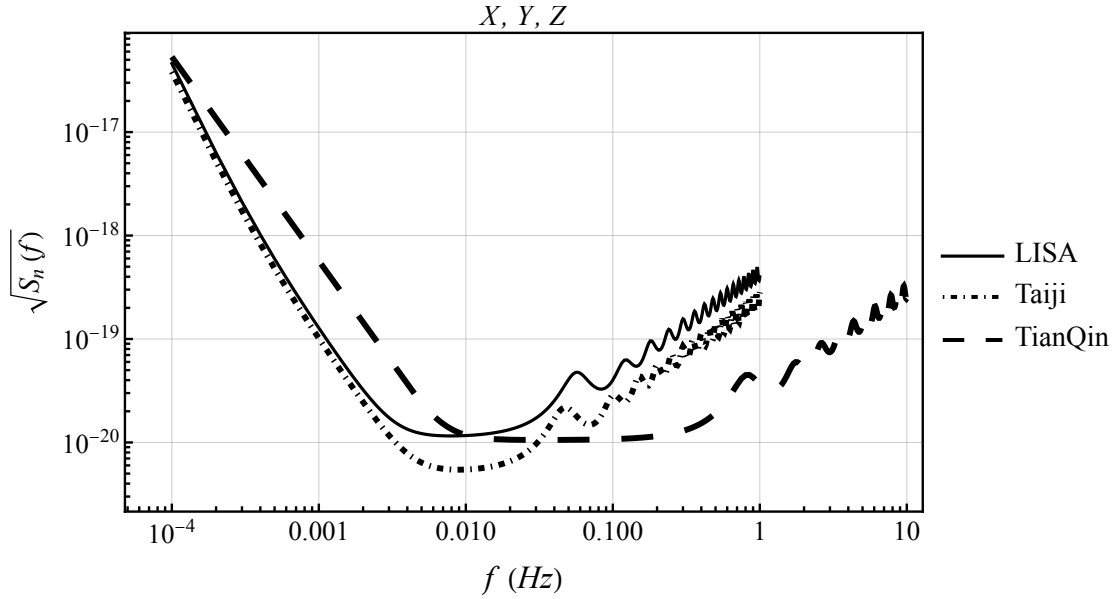


Figure 6. The sensitivity curves of LISA, Taiji and TianQin with the Michelson (X, Y, Z) combination.

The mean value of $\Delta\Omega_s$				
f (Hz)	LISA	Taiji	TianQin	Network
0.001	2.6849×10^{-3} (2.6881×10^{-3})	1.3030×10^{-3} (1.3055×10^{-3})	9.1255×10^{-2} (9.1256×10^{-2})	6.1312×10^{-4} (6.1410×10^{-4})
0.01	3.6733×10^{-5} (3.6890×10^{-5})	7.8631×10^{-6} (8.0162×10^{-6})	4.1719×10^{-5} (4.1725×10^{-5})	4.3272×10^{-6} (4.3838×10^{-6})
0.1	3.0966×10^{-7} (3.1250×10^{-7})	1.5947×10^{-7} (1.5947×10^{-7})	2.3068×10^{-8} (2.3068×10^{-8})	1.6795×10^{-8} (1.6808×10^{-8})
The median value of $\Delta\Omega_s$				
f (Hz)	LISA	Taiji	TianQin	Network
0.001	2.5871×10^{-3} (2.59021×10^{-3})	1.3051×10^{-3} (1.3076×10^{-3})	5.1638×10^{-2} (5.1638×10^{-2})	6.0841×10^{-4} (6.0939×10^{-4})
0.01	2.7778×10^{-5} (2.79001×10^{-5})	5.7658×10^{-6} (5.8981×10^{-6})	2.3607×10^{-5} (2.3610×10^{-5})	2.8500×10^{-6} (2.8856×10^{-6})
0.1	1.6370×10^{-7} (1.6521×10^{-7})	7.1032×10^{-8} (7.1032×10^{-8})	1.3014×10^{-8} (1.3014×10^{-8})	8.8234×10^{-9} (8.8313×10^{-9})

Table 3. The mean and median values of angular resolutions $\Delta\Omega_s$ for space-based GW detectors and their network with Michelson (X, Y, Z) combination and without TDI, the results in brackets are for those without TDI.

With the same detector, the ratios between the mean values of the angular resolutions with and without TDI for different TDI combinations equal to $S_n^{\text{TDI}}/S_n^{\text{no-TDI}}$. For the effect of the detector's changing orientation on the sky localization with different TDI combinations, we find that the ratio of the mean values of the angular resolutions between the fiducial detectors C and R is approximately 2.24 at $f_0 = 1$ mHz, 1.1 at $f_0 = 0.01$ Hz and $f_0 = 0.1$

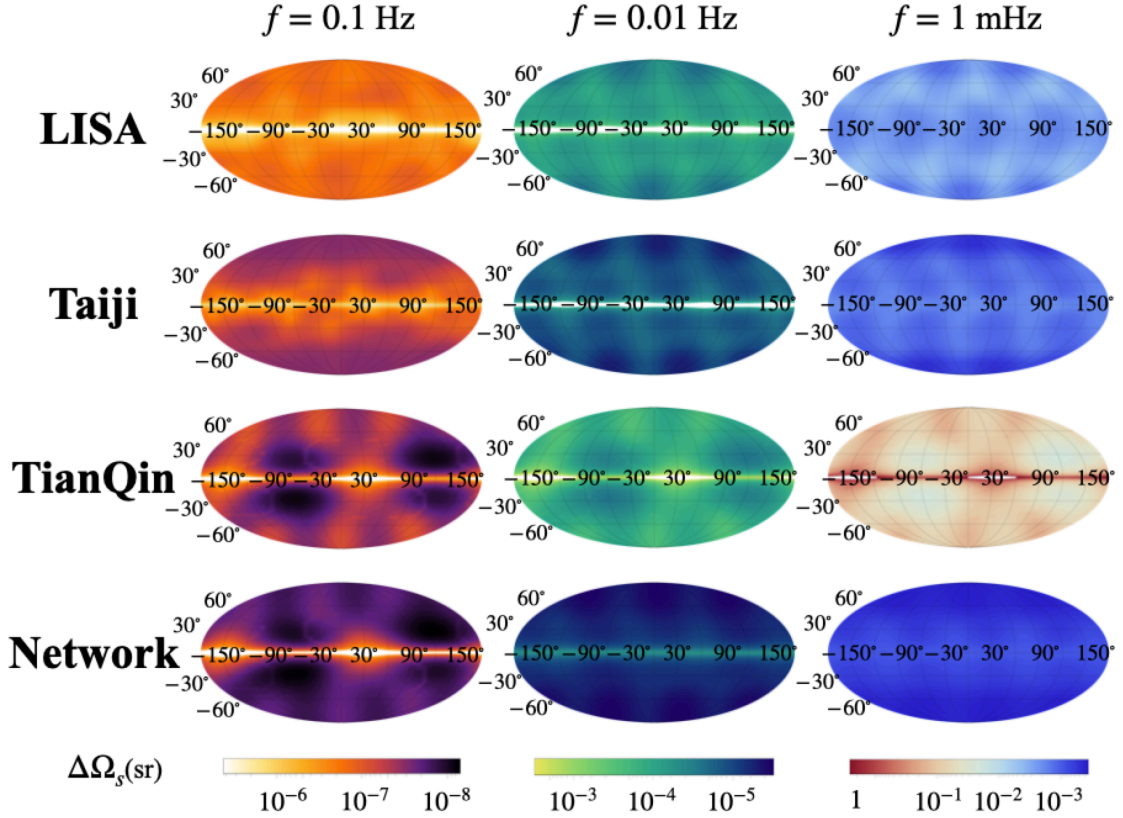


Figure 7. The sky map of angular resolutions in the unit of steradian for LISA, Taiji, TianQin, and the LISA-Taiji-TianQin network with the TDI (X, Y, Z) combination. From left to right, the frequencies are 0.1 Hz, 0.01 Hz and 1 mHz.

Hz for all TDI combinations including no-TDI. For the effect of the orbital period on the sky localization with different TDI combinations, we find that the ratio of the mean values of the angular resolutions between the fiducial detectors C1 and C2 is approximately 1 at the three frequencies for all TDI combinations. The effect of the arm length is reflected in the sensitivity curve through the noise and the transfer function, we find that the ratio between the mean value of the angular resolutions with detectors 1 and 2 is $\Delta\Omega_{s,1}/\Delta\Omega_{s,2} = S_{n,1}/S_{n,2}$ for all TDI combinations. Therefore, we conclude that the influence of different TDI combination on the sky localization mainly comes from the sensitivity curve of the detector with the TDI combination.

Since the sensitivity with the (X, Y, Z) combination is better, we apply the (X, Y, Z) combination to analyze the uncertainty of sky localization for LISA, Taiji, TianQin and the LISA-Taiji-TianQin network. At the low frequency $f_0 = 1$ mHz, the mean value of the angular resolutions with LISA is better than that with TianQin by about 34 times of magnitude with the help of the noise curve, Taiji is two times better than LISA, and the LISA-Taiji-TianQin network is 2.5 times better than Taiji. At the medium frequency $f_0 = 0.01$ Hz, the mean value of the angular resolutions with LISA is less than two times better than that with TianQin, Taiji is almost five times better than LISA, and the LISA-Taiji-TianQin network is less than two times better than Taiji. At the relatively high frequency $f_0 = 0.1$ Hz, the mean value of the angular resolutions with Taiji is two times better than that with LISA, TianQin is seven

times better than Taiji, and the LISA-Taiji-TianQin network is around ten times better than Taiji.

For monochromatic sources, the detector in different orbital positions can be thought as an independent detector, so the improvement on the angular resolutions by the network of combined detectors is small. The mean values of angular resolutions with the LISA-Taiji-TianQin network are about 6.1×10^{-4} steradian at 1 mHz, 4.3×10^{-6} steradian at 10 mHz and 1.7×10^{-8} steradian at 100 mHz. The difference between the angular resolutions with the (X, Y, Z) combination and without TDI is less than 14%.

This analysis is based on the first-generation TDI with constant arm length, the effect of time-changing arm length can be dealt with the second-generation TDI combinations and this will be our future study. Furthermore, we use the uncorrelated noise model in this paper to simplify the calculation, the realistic noise model for space-based GW detectors is complicated, and it should be carefully studied in the future.

Acknowledgments

This research is supported in part by the National Key Research and Development Program of China under Grant No. 2020YFC2201504 and the National Natural Science Foundation of China (NSFC) under Grant NO.12465013.

References

- [1] LIGO SCIENTIFIC, VIRGO collaboration, *Observation of Gravitational Waves from a Binary Black Hole Merger*, *Phys. Rev. Lett.* **116** (2016) 061102 [[1602.03837](#)].
- [2] LIGO SCIENTIFIC collaboration, *Advanced LIGO: The next generation of gravitational wave detectors*, *Class. Quant. Grav.* **27** (2010) 084006.
- [3] LIGO SCIENTIFIC collaboration, *Advanced LIGO*, *Class. Quant. Grav.* **32** (2015) 074001 [[1411.4547](#)].
- [4] VIRGO collaboration, *Advanced Virgo: a second-generation interferometric gravitational wave detector*, *Class. Quant. Grav.* **32** (2015) 024001 [[1408.3978](#)].
- [5] LIGO SCIENTIFIC, VIRGO collaboration, *Tests of general relativity with GW150914*, *Phys. Rev. Lett.* **116** (2016) 221101 [[1602.03841](#)].
- [6] LIGO SCIENTIFIC, VIRGO collaboration, *Tests of General Relativity with GW170817*, *Phys. Rev. Lett.* **123** (2019) 011102 [[1811.00364](#)].
- [7] LIGO SCIENTIFIC, VIRGO collaboration, *Tests of General Relativity with the Binary Black Hole Signals from the LIGO-Virgo Catalog GWTC-1*, *Phys. Rev. D* **100** (2019) 104036 [[1903.04467](#)].
- [8] LIGO SCIENTIFIC, VIRGO collaboration, *Tests of general relativity with binary black holes from the second LIGO-Virgo gravitational-wave transient catalog*, *Phys. Rev. D* **103** (2021) 122002 [[2010.14529](#)].
- [9] LIGO SCIENTIFIC, VIRGO collaboration, *Binary Black Hole Mergers in the first Advanced LIGO Observing Run*, *Phys. Rev. X* **6** (2016) 041015 [[1606.04856](#)].
- [10] LIGO SCIENTIFIC, VIRGO collaboration, *The Rate of Binary Black Hole Mergers Inferred from Advanced LIGO Observations Surrounding GW150914*, *Astrophys. J. Lett.* **833** (2016) L1 [[1602.03842](#)].

- [11] LIGO SCIENTIFIC, VIRGO collaboration, *Upper Limits on the Rates of Binary Neutron Star and Neutron Star–black Hole Mergers From Advanced Ligo’s First Observing run*, *Astrophys. J. Lett.* **832** (2016) L21 [[1607.07456](#)].
- [12] LIGO SCIENTIFIC, VIRGO, KAGRA collaboration, *Constraints on the Cosmic Expansion History from GWTC–3*, *Astrophys. J.* **949** (2023) 76 [[2111.03604](#)].
- [13] N. Seto, S. Kawamura and T. Nakamura, *Possibility of direct measurement of the acceleration of the universe using 0.1-Hz band laser interferometer gravitational wave antenna in space*, *Phys. Rev. Lett.* **87** (2001) 221103 [[astro-ph/0108011](#)].
- [14] K. Kyutoku and N. Seto, *Gravitational-wave cosmography with LISA and the Hubble tension*, *Phys. Rev. D* **95** (2017) 083525 [[1609.07142](#)].
- [15] ELISA collaboration, *The Gravitational Universe*, [1305.5720](#).
- [16] A. Klein et al., *Science with the space-based interferometer eLISA: Supermassive black hole binaries*, *Phys. Rev. D* **93** (2016) 024003 [[1511.05581](#)].
- [17] A. Sesana, M. Volonteri and F. Haardt, *LISA detection of massive black hole binaries: imprint of seed populations and of extreme recoils*, *Class. Quant. Grav.* **26** (2009) 094033 [[0810.5554](#)].
- [18] A. Ricarte and P. Natarajan, *The Observational Signatures of Supermassive Black Hole Seeds*, *Mon. Not. Roy. Astron. Soc.* **481** (2018) 3278 [[1809.01177](#)].
- [19] K. Li, T. Bogdanović, D. R. Ballantyne and M. Bonetti, *Massive Black Hole Binaries from the TNG50-3 Simulation. I. Coalescence and LISA Detection Rates*, *Astrophys. J.* **933** (2022) 104 [[2201.11088](#)].
- [20] A. Mangiagli, C. Caprini, M. Volonteri, S. Marsat, S. Vergani, N. Tamanini et al., *Massive black hole binaries in LISA: Multimessenger prospects and electromagnetic counterparts*, *Phys. Rev. D* **106** (2022) 103017 [[2207.10678](#)].
- [21] K. Danzmann, *LISA: An ESA cornerstone mission for a gravitational wave observatory*, *Class. Quant. Grav.* **14** (1997) 1399.
- [22] LISA collaboration, *Laser Interferometer Space Antenna*, [1702.00786](#).
- [23] W.-R. Hu and Y.-L. Wu, *The Taiji Program in Space for gravitational wave physics and the nature of gravity*, *Natl. Sci. Rev.* **4** (2017) 685.
- [24] TIANQIN collaboration, *TianQin: a space-borne gravitational wave detector*, *Class. Quant. Grav.* **33** (2016) 035010 [[1512.02076](#)].
- [25] K. Grover, S. Fairhurst, B. F. Farr, I. Mandel, C. Rodriguez, T. Sidery et al., *Comparison of Gravitational Wave Detector Network Sky Localization Approximations*, *Phys. Rev. D* **89** (2014) 042004 [[1310.7454](#)].
- [26] C. Cutler, *Angular resolution of the LISA gravitational wave detector*, *Phys. Rev. D* **57** (1998) 7089 [[gr-qc/9703068](#)].
- [27] C. P. L. Berry et al., *Parameter estimation for binary neutron-star coalescences with realistic noise during the Advanced LIGO era*, *Astrophys. J.* **804** (2015) 114 [[1411.6934](#)].
- [28] B. F. Schutz, *Determining the Hubble Constant from Gravitational Wave Observations*, *Nature* **323** (1986) 310.
- [29] D. E. Holz and S. A. Hughes, *Using gravitational-wave standard sirens*, *Astrophys. J.* **629** (2005) 15 [[astro-ph/0504616](#)].
- [30] H.-Y. Chen, M. Fishbach and D. E. Holz, *A two per cent Hubble constant measurement from standard sirens within five years*, *Nature* **562** (2018) 545 [[1712.06531](#)].

- [31] K. Hotokezaka, E. Nakar, O. Gottlieb, S. Nissanke, K. Masuda, G. Hallinan et al., *A Hubble constant measurement from superluminal motion of the jet in GW170817*, *Nature Astron.* **3** (2019) 940 [1806.10596].
- [32] S. Vitale and H.-Y. Chen, *Measuring the Hubble constant with neutron star black hole mergers*, *Phys. Rev. Lett.* **121** (2018) 021303 [1804.07337].
- [33] LIGO SCIENTIFIC, VIRGO, VIRGO collaboration, *A Gravitational-wave Measurement of the Hubble Constant Following the Second Observing Run of Advanced LIGO and Virgo*, *Astrophys. J.* **909** (2021) 218 [1908.06060].
- [34] L.-G. Zhu, L.-H. Xie, Y.-M. Hu, S. Liu, E.-K. Li, N. R. Napolitano et al., *Constraining the Hubble constant to a precision of about 1% using multi-band dark standard siren detections*, *Sci. China Phys. Mech. Astron.* **65** (2022) 259811 [2110.05224].
- [35] A. G. Riess, S. Casertano, W. Yuan, L. M. Macri and D. Scolnic, *Large Magellanic Cloud Cepheid Standards Provide a 1% Foundation for the Determination of the Hubble Constant and Stronger Evidence for Physics beyond Λ CDM*, *Astrophys. J.* **876** (2019) 85 [1903.07603].
- [36] A. Blaut, *Accuracy of estimation of parameters with LISA*, *Phys. Rev. D* **83** (2011) 083006.
- [37] C. Zhang, N. Dai and D. Liang, *Importance of including higher signal harmonics in the modeling of extreme mass-ratio inspirals*, *Phys. Rev. D* **108** (2023) 044076 [2306.13871].
- [38] C. Zhang, Y. Gong, H. Liu, B. Wang and C. Zhang, *Sky localization of space-based gravitational wave detectors*, *Phys. Rev. D* **103** (2021) 103013 [2009.03476].
- [39] C. Zhang, Y. Gong, B. Wang and C. Zhang, *Accuracy of parameter estimations with a spaceborne gravitational wave observatory*, *Phys. Rev. D* **103** (2021) 104066 [2012.01043].
- [40] Y. Gong, J. Luo and B. Wang, *Concepts and status of Chinese space gravitational wave detection projects*, *Nature Astron.* **5** (2021) 881 [2109.07442].
- [41] M. Peterseim, O. Jennrich and K. Danzmann, *Accuracy of parameter estimation of gravitational waves with LISA*, *Class. Quant. Grav.* **13** (1996) A279.
- [42] M. Tinto, G. Giampieri, R. W. Hellings, P. L. Bender and J. E. Faller, *Algorithms for unequal-arm Michelson interferometers*, in *7th Marcel Grossmann Meeting on General Relativity (MG 7)*, pp. 1668–1670, 7, 1994.
- [43] M. Tinto and J. W. Armstrong, *Cancellation of laser noise in an unequal-arm interferometer detector of gravitational radiation*, *Phys. Rev. D* **59** (1999) 102003.
- [44] J. W. Armstrong, F. B. Estabrook and M. Tinto, *Time-delay interferometry for space-based gravitational wave searches*, *Astrophys. J.* **527** (1999) 814.
- [45] F. B. Estabrook, M. Tinto and J. W. Armstrong, *Time delay analysis of LISA gravitational wave data: Elimination of spacecraft motion effects*, *Phys. Rev. D* **62** (2000) 042002.
- [46] M. Tinto, F. B. Estabrook and J. W. Armstrong, *Time delay interferometry with moving spacecraft arrays*, *Phys. Rev. D* **69** (2004) 082001 [gr-qc/0310017].
- [47] M. Vallisneri, *Synthetic LISA: Simulating time delay interferometry in a model LISA*, *Phys. Rev. D* **71** (2005) 022001 [gr-qc/0407102].
- [48] D. A. Shaddock, M. Tinto, F. B. Estabrook and J. W. Armstrong, *Data combinations accounting for LISA spacecraft motion*, *Phys. Rev. D* **68** (2003) 061303 [gr-qc/0307080].
- [49] N. J. Cornish and R. W. Hellings, *The Effects of orbital motion on LISA time delay interferometry*, *Class. Quant. Grav.* **20** (2003) 4851 [gr-qc/0306096].
- [50] M. Tinto, J. W. Armstrong and F. B. Estabrook, *Discriminating a gravitational wave background from instrumental noise in the LISA detector*, *Phys. Rev. D* **63** (2001) 021101.

- [51] M. Tinto, J. W. Armstrong and F. B. Estabrook, *Discriminating a gravitational-wave background from instrumental noise using time-delay interferometry*, *Class. Quant. Grav.* **18** (2001) 4081.
- [52] C. J. Hogan and P. L. Bender, *Estimating stochastic gravitational wave backgrounds with Sagnac calibration*, *Phys. Rev. D* **64** (2001) 062002 [[astro-ph/0104266](#)].
- [53] J. W. Armstrong, F. B. Estabrook and M. Tinto, *Sensitivities of alternate LISA configurations*, *Class. Quant. Grav.* **18** (2001) 4059.
- [54] T. A. Prince, M. Tinto, S. L. Larson and J. W. Armstrong, *The LISA optimal sensitivity*, *Phys. Rev. D* **66** (2002) 122002 [[gr-qc/0209039](#)].
- [55] M. Tinto, F. B. Estabrook and J. W. Armstrong, *Time delay interferometry for LISA*, *Phys. Rev. D* **65** (2002) 082003.
- [56] M. Tinto, D. A. Shaddock, J. Sylvestre and J. W. Armstrong, *Implementation of time delay interferometry for LISA*, *Phys. Rev. D* **67** (2003) 122003 [[gr-qc/0303013](#)].
- [57] K. R. Nayak, S. V. Dhurandhar, A. Pai and J. Y. Vinet, *Optimizing the directional sensitivity of LISA*, *Phys. Rev. D* **68** (2003) 122001 [[gr-qc/0306050](#)].
- [58] M. Tinto and S. L. Larson, *The LISA time-delay interferometry zero-signal solution. I. Geometrical properties*, *Phys. Rev. D* **70** (2004) 062002 [[gr-qc/0405147](#)].
- [59] J. D. Romano and G. Woan, *A Principal component analysis for LISA: The TDI connection*, *Phys. Rev. D* **73** (2006) 102001 [[gr-qc/0602033](#)].
- [60] C. Zhang, Q. Gao, Y. Gong, B. Wang, A. J. Weinstein and C. Zhang, *Full analytical formulas for frequency response of space-based gravitational wave detectors*, *Phys. Rev. D* **101** (2020) 124027 [[2003.01441](#)].
- [61] A. Krolak, M. Tinto and M. Vallisneri, *Optimal filtering of the LISA data*, *Phys. Rev. D* **70** (2004) 022003 [[gr-qc/0401108](#)].
- [62] M. Vallisneri, *Geometric time delay interferometry*, *Phys. Rev. D* **72** (2005) 042003 [[gr-qc/0504145](#)].
- [63] G. Wang and W.-T. Ni, *Numerical simulation of time delay interferometry for TAIJI and new LISA*, *Res. Astron. Astrophys.* **19** (2019) 058 [[1707.09127](#)].
- [64] G. Wang and W.-T. Ni, *Revisiting time delay interferometry for unequal-arm LISA and TAIJI*, *Phys. Scripta* **98** (2023) 075005 [[2008.05812](#)].
- [65] G. Wang, W.-T. Ni, W.-B. Han and C.-F. Qiao, *Algorithm for time-delay interferometry numerical simulation and sensitivity investigation*, *Phys. Rev. D* **103** (2021) 122006 [[2010.15544](#)].
- [66] K. Rajesh Nayak and J. Y. Vinet, *Algebraic approach to time-delay data analysis for orbiting LISA*, .
- [67] K. R. Nayak and J. Y. Vinet, *Algebraic approach to time-delay data analysis: Orbiting case*, *Class. Quant. Grav.* **22** (2005) S437.
- [68] M. Tinto and S. V. Dhurandhar, *TIME DELAY*, *Living Rev. Rel.* **8** (2005) 4 [[gr-qc/0409034](#)].
- [69] M. Tinto and S. V. Dhurandhar, *Time-Delay Interferometry*, *Living Rev. Rel.* **17** (2014) 6.
- [70] M. Tinto and S. V. Dhurandhar, *Time-delay interferometry*, *Living Rev. Rel.* **24** (2021) 1.
- [71] M. Muratore, D. Vetrugno and S. Vitale, *Revisitation of time delay interferometry combinations that suppress laser noise in LISA*, *Class. Quant. Grav.* **37** (2020) 185019 [[2001.11221](#)].
- [72] S. L. Larson, R. W. Hellings and W. A. Hiscock, *Unequal arm space borne gravitational wave detectors*, *Phys. Rev. D* **66** (2002) 062001 [[gr-qc/0206081](#)].

- [73] N. J. Cornish and S. L. Larson, *Space missions to detect the cosmic gravitational wave background*, *Class. Quant. Grav.* **18** (2001) 3473 [[gr-qc/0103075](#)].
- [74] T. Robson, N. J. Cornish and C. Liu, *The construction and use of LISA sensitivity curves*, *Class. Quant. Grav.* **36** (2019) 105011 [[1803.01944](#)].
- [75] M. Vallisneri, J. Crowder and M. Tinto, *Sensitivity and parameter-estimation precision for alternate LISA configurations*, *Class. Quant. Grav.* **25** (2008) 065005 [[0710.4369](#)].
- [76] M. Muratore, O. Hartwig, D. Vetrugno, S. Vitale and W. J. Weber, *Effectiveness of null time-delay interferometry channels as instrument noise monitors in LISA*, *Phys. Rev. D* **107** (2023) 082004 [[2207.02138](#)].
- [77] D. Q. Nam, Y. Lemiere, A. Petiteau, J.-B. Bayle, O. Hartwig, J. Martino et al., *TDI noises transfer functions for LISA*, [2211.02539](#).
- [78] C. Zhang, Q. Gao, Y. Gong, D. Liang, A. J. Weinstein and C. Zhang, *Frequency response of time-delay interferometry for space-based gravitational wave antenna*, *Phys. Rev. D* **100** (2019) 064033 [[1906.10901](#)].
- [79] A. Vecchio and E. D. L. Wickham, *The Effect of the LISA response function on observations of monochromatic sources*, *Phys. Rev. D* **70** (2004) 082002 [[gr-qc/0406039](#)].